Article
journal of Studies of Earth's Deep Interior
doi:10.46298/jsedi.15652

Influence of background magnetic fields on the excitation of Magneto-Coriolis modes inside the Earth's core

O. Barrois * [1], **J. Aubert** [1]

[1] Université de Paris, Institut de Physique du Globe de Paris, CNRS, F-75005 Paris, France

Author contributions: *Conceptualization*: J. Aubert, O. Barrois. *Methodology*: J. Aubert. *Formal Analysis*: O. Barrois. *Writing - Original draft*: O. Barrois. *Writing - Review & Editing*: O. Barrois, J. Aubert.

Abstract Magneto-Coriolis (QG-MC) waves are considered an important part of the rapid dynamics of the Earth's outer core. The detailed characteristics of these waves are however still under scrutiny. In this study we explore the sensitivity of the QG-MC waves to the background magnetic field over which they propagate and to the frequency of a periodic perturbation that we impose. We retrieve QG-MC modes by analysing the velocity fields, where they are most easily observed. Concentrations of QG-MC waves in the magnetic field at the core surface in our model are reminiscent of recently observed geomagnetic jerks. The QG-MC waves are weakly sensitive to the details of the background magnetic field during their travel in the bulk and their frequency at the core surface remains close to that of the initial perturbation. This is a potential asset for the prediction of their evolution. Moreover, the waves in the system exhibit a complex relation with the initial perturbation: when the frequency of the initial pulsation is greater than a threshold – depending on the Alfvén speed of the medium – inward QG-Alfvén waves are recovered at the core mantle boundary instead of QG-MC waves, and we find that the waves evolve from QG-MC to QG-Alfvén waves depending on the input frequency. Thus, gradually increasing the input frequency in the system, we retrieve the dispersion relation for QG-MC waves with an evolution from a k_s^4 slope to a k_s^1 slope, where k_s is the cylindrical radial wavenumber, as waves transition from QG-MC to QG-Alfvén waves. We actually recover all the components of the dispersion relation from QG-MC waves at low pulsation ω to QG-Alfvén and inertial waves at high pulsation ω. Applying our results to the Earth's core, we expect to be able to recover QG-MC waves with confidence in the Earth's core with periods between 57 y and 2.8 y.

Handling Editor: Mathieu Dumberry
Received: May 12, 2025
Revised: July 25, 2025; October 1, 2025
Accepted: October 2, 2025
Published: October 23, 2025

1 Introduction

The rapid dynamics of the geomagnetic field – from inter-annual up to decadal timescales – is driven by hydromagnetic waves, including Quasi-Geostrophic Magneto-Coriolis (QG-MC) waves which have been recently reconsidered as instrumental at these timescales. QG-MC waves with different periods have been observed in velocity time series inferred from the geomagnetic signals (Gillet, Gerick, Jault, et al., 2022; Istas et al., 2023) after having been discovered at inter-annual periods (Gerick et al., 2021). Their timescales are much shorter than the convection, or overturn, timescale of the core $\tau_u = d/U_c \approx 125\,\mathrm{y}$, with $U_c \approx 18\,\mathrm{km/y}$ a typical convective velocity of the fluid core, and with $d = 2260\,\mathrm{km}$ the thickness of the Earth's core, and much longer than the rotation timescale of the core $2\pi\,\tau_\Omega = 2\pi/\Omega = 1\,\mathrm{day}$, with Ω the rotation period of the Earth. Their fundamental timescale is the Alfvén time of the core $\tau_\mathcal{A} = d\sqrt{\rho\,\mu}/B_\oplus$, where $\rho \simeq 10^4\,\mathrm{kg/m^3}$ and $\mu = 4\pi \times 10^{-7}\,\mathrm{H/m}$ are respectively the density and the magnetic permeability of the fluid, and $B_\oplus$ is the rms strength of the Earth's magnetic field. The Alfvén time for the Earth's outer core has an estimated value of $\tau_\mathcal{A} \simeq 2\,y$ obtained from an rms field strength of $B_\oplus \sim 4\,\mathrm{mT}$ (Gillet et al., 2010).

In recent years, the improvement of the geomagnetic field models (*e.g.*, Finlay et al., 2020; Lesur et al., 2022), and the use of data assimilation techniques to predict the evolution of the geomagnetic field (Barrois et al., 2018; Aubert, 2020; Istas et al., 2023) has produced satisfactory results to explain the signals recovered at the core mantle boundary (CMB). But the fundamental question about the possibility of improving our predictions compared to a simple extrapolation (Alken et al., 2021) remains. Looking at periodic signals in the geomagnetic data (*e.g.*, Gillet et al., 2015; Buffett and Matsui, 2019) and using hydrodynamics waves to probe the Earth's core interior is not new and some waves like the torsional Alfvén waves have given good insights on both the length-of-day and the core surface flows dynamics (Gillet et al., 2010) even if these torsional Alfvén waves do not account for all of the inter-annual geomagnetic signals (Chulliat and Maus, 2014). More generally, the study of a variety of periodic signals found in the geophysical records have provided insightful knowledge on the otherwise directly inaccessible deep layers of the Earth (Rekier et al., 2022; Triana et al., 2022; Rosat and Gillet, 2023; Schwaiger et al., 2024; Cazenave et al., 2025). With the recently discovered QG-MC waves of suitable periods which could be sensible to the long term velocity and magnetic fields (*e.g.*, Gerick and Livermore, 2024), hopes

*Corresponding author: obarrois@ipgp.fr

are it would potentially unlock a new level of understanding on the deep structure of the Earth's core and allow for an improvement of our predictions (Gillet, Gerick, Jault, et al., 2022). This question is directly relevant in our present study and is one of the main motivations underlying this work.

Our approach builds upon 3D model computations (*e.g.*, Aubert, 2023) in a reduced framework taking advantage of the timescales separation between the slow secular processes and the fast inter-annual dynamics of the Earth's core, which is a common strategy for studying axisymmetric or non-axisymmetric perturbations and for characterising the rapid dynamics of the geodynamo system (Jault, 2008; Gillet et al., 2011; Gerick et al., 2021). Considering that the slower convective dynamics is static compared to the inter-annual waves, we adopt a perturbation approach and linearise the dynamics equations around a stationary background state which ensures the timescales separation of the different processes. This is a continuation of our previous work (Barrois and Aubert, 2024) as we add more complexity by using a more geophysical background magnetic field from the path model dynamo models (Aubert et al., 2017). We also study the response of the system to a monochromatic periodic forcing instead of its impulsional response.

The paper is organised as follows. We briefly describe the context and the geophysical background field used in our study in Section 2, then present our results in Section 3, before discussing and providing the conclusions of this work in Section 4. More details are given about the methodology of our study in Appendix A.

2 Methods

2.1 System solved

In this study, we follow Jault, 2008; Barrois and Aubert, 2024 and use a reduced system of equations (see Methods details A.1, Eq. 8-9) linearised around an arbitrary background velocity field $\mathbf{U}_0$ and a chosen background magnetic field $\mathbf{B}_0$ (see Fig. 1). Our model describes the dynamics of a rapidly rotating thick spherical shell filled with a conducting incompressible fluid and solves for the velocity field $\mathbf{U}$ and the magnetic field $\mathbf{B}$ of this fluid. More precisely, it solves for the velocity perturbation $\boldsymbol{u}$ and magnetic perturbation $\mathbf{b}$ fields, *i.e.* $\mathbf{U} \equiv \mathbf{U}_0 + \boldsymbol{u}$, although the background flow $\mathbf{U}_0$ is neglected as the studied waves are fast compared to the average outer core's speed (see Appendix A.1), and $\mathbf{B} \equiv \mathbf{B}_0 + \mathbf{b}$. We make use of the spherical coordinates system (r, θ, ϕ) with unit vectors $(\boldsymbol{e}_r, \boldsymbol{e}_\theta, \boldsymbol{e}_\phi)$, even though the cylindrical coordinates system (s, ϕ, z) with unit vectors $(\boldsymbol{e}_s, \boldsymbol{e}_\phi, \boldsymbol{e}_z)$ might alternatively be used to describe the quantities. The thick shell is assumed to have a thickness $d = r_o - r_i$ with an aspect ratio $r_i/r_o = 0.35$, with $r_o = 3,485\,\text{km}$ and $r_i = 1,225\,\text{km}$ respectively the outer and inner core surface radii, rotating at a constant angular velocity aligned with the rotation axis $\boldsymbol{\Omega} = \Omega \boldsymbol{e}_z$, which reflects the outer core of the Earth. A solid inner core is included in the system, which is able to rotate independently (the full kinetic momentum is conserved), and which has the same electrical conductivity as that of the outer core, $\sigma \simeq 0.5 \times 10^6\,\text{S.m}^{-1}$ (*e.g.*, Gillet et al., 2010; Pozzo and Alfè, 2016). The boundary conditions are insulating at $r = r_o$ and conducting at $r = r_i$ for the magnetic field, and are stress-free at both r_i and r_o for the velocity field.

We focus here on a series of simulations conducted at moderate parameters aiming at reproducing the Earth's core conditions and the observed geomagnetic waves, *i.e.* with a high rotation rate, a strong magnetic field and a low level of attenuation. More details about our methodology and the equations of our system can be found in the Appendix A.1.

2.2 Magnetic base state

In order to best represent the magnetic structure of the Earth's core, we use a data assimilation based recent inference of the magnetic field inside the Earth's core. Specifically, we use the ensemble mean of sequence A from Aubert, 2023 at epoch 2000. Figure 1 displays the main characteristics of this background field $\mathbf{B}_0$ that, by construction, matches the present geomagnetic field at the CMB (as can be seen in Fig. 1 a) and retains the properties of the dynamo model in its interior (Fig. 1 b-c). This background state is highly heterogeneous and carries non-symmetric components, although it remains mostly dipolar.

Note that, as a reference, we also use a simple background magnetic field from Barrois and Aubert, 2024 (which is non-axisymmetric, has a non-zero $B^2_{0,r}$ component at the equator, and matches a potential at the outer boundary, see their Fig. 1) and remember that we neglect the background velocity field in all configurations (see A.1). Figure 2 compares the spectral structure of the complex and simple background magnetic fields as a function of the spherical harmonic order m and we can readily see that the complex background magnetic field allows for coupling between all m and ℓ in the system contrary to the simple background which only allows for waves with azimuthal symmetries that are multiples of $m = 3$.

Respectively, the cases computed using the simple background are labeled Cases S and the cases computed using the complex background are labeled Cases C in Table 1 (Appendix B) which reference all our simulations. In the following, we will focus on and compare several specific cases: two cases computed at the same input period $T_i = 4.4\,\text{y}$ using the simple and the complex background states, Cases SB-1 and CB-1 respectively, a case computed at a faster input period $T_i = 0.6\,\text{y}$ using the complex background state, Case CB-2, and a case computed at an even faster input period $T_i = 0.06\,\text{y} \approx 22\,\text{d}$ using the complex background state, Case CB-3.

2.3 Initial conditions

At the start of our computations, the system is at rest with respect to the reference frame of rotation. To set the system in motion, a non-axisymmetric monochromatic periodic forcing is imposed in the force balance just above r_i. Note that we chose to excite waves in the current setup by introducing an additional force to represent the slight imbalances in the dominant QG-MAC force balance that excite waves in the Earth's core (*e.g.*, Aubert and Gillet, 2021). The periodic perturbation function $\mathcal{F}_p$ is set at a specific sectorial spherical harmonic, Gaussian in the radial direction and periodic in time, such that

$$\mathcal{F}_p(r,\theta,\phi,t) = \frac{1}{\sqrt{2\pi}\,\Sigma^*} \exp\left\{-\frac{1}{2}\left(\frac{r-r_i}{\Sigma^*}\right)^2\right\} Y_3^3(\theta,\phi)\,\sin(\omega_i\, t), \tag{1}$$

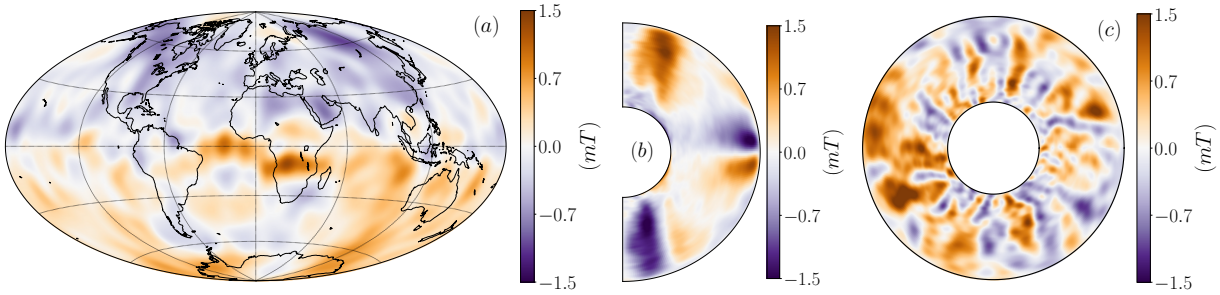

Figure 1: Complex background magnetic field $\mathbf{B}_0$ used in this study: (a) radial component of the magnetic field $B_{0,r}$ at the core surface, (b) axisymmetric azimuthal magnetic field $\frac{1}{2\pi}\int_0^{2\pi} B_{0,\phi}\,\mathrm{d}\phi$, (c) and $B_{0,r}$ in the equatorial plane.

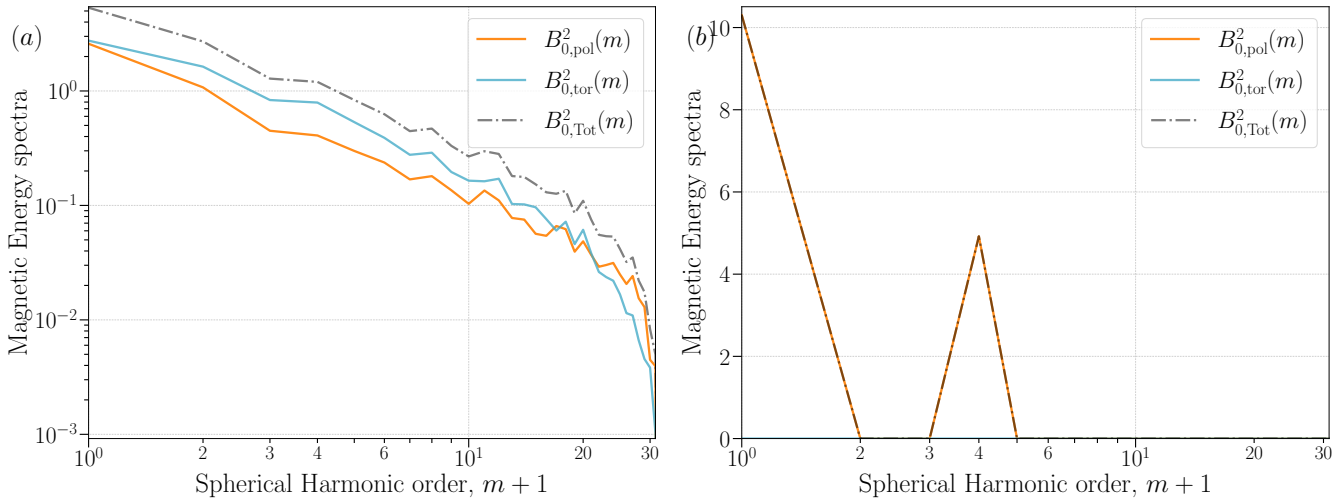

Figure 2: Power spectra as a function of the spherical harmonic order m of the the poloidal (orange curves) and the toroidal (light blue curves) components of the Complex background magnetic field (a) and the Simple background magnetic field (b) both truncated at harmonic order $m_{\mathrm{cut}} = 30$.

where the $Y_\ell^m(\theta,\phi)$ are the spherical harmonics into which both the velocity and magnetic fields are decomposed, with ℓ and m respectively the spherical harmonic degree and order of the decomposition, $\Sigma^* = 0.01$ controls the sharpness of the Gaussian, and ω_i is the input pulsation of the system which is a free parameter that controls the frequency of the perturbation, reported in Table 1 (Appendix B) for our set of simulations (expressed in dimensionless Alfvén times). Note that the input pulsation is related to the input period with the relation $\omega_i = 2\pi/T_i$.

We chose a sectorial $\ell = m = 3$ harmonic following the idea that most perturbations are expected to be sectorial because of the overall equatorially symmetric dynamics of the Earth's core (*e.g.*, Aubert, 2023). Moreover, the complexity of the geophysical background allows for a mixing of all modes.

This is a direct follow-up to our previous work (Barrois and Aubert, 2024) as we focus here on the periodic response of the system when using a complex background magnetic field mainly to retrieve the dispersion relation of the QG-MC normal modes, and to draw parallels between the steady state of our reduced model and periodic signals retrieved in the geomagnetic records (*e.g.*, Gillet, Gerick, Jault, et al., 2022).

3 Results

The periodic perturbation is enabled at $t = 0$ and we wait for a steady state to take place in the simulations, usually after a time corresponding to a few years, before analysing the results that are presented throughout this section. Note that the input parameters and some additional observations for all our 23 simulations are reported in Table 1 (Appendix B). We have focused here on simulations parameters that are relevant for the Earth's core and the geomagnetic data, *i.e.* with input periods ranging from a fraction of a year to a few decades, and in the high rotation, low dissipation regime – which is already sufficiently enforced at these parameters (Barrois and Aubert, 2024) so it allows for covering a wide part of the parameters space at a limited computational cost.

3.1 Response to a periodic forcing

For Case CB-1, using a forcing period corresponding to $T_i = 4.4\,\mathrm{y}$ and the background magnetic field of Fig. 1, snapshots of the azimuthal velocity at the core surface (Fig. 3 a) reveal the wedged patterns that focus on the equator which are characteristic of QG-MC waves (Gillet, Gerick, Jault, et al., 2022; Gerick and Livermore, 2024). In the radial magnetic field (Fig. 3 b) the QG-MC waves signature take the form of irregular patches mostly found at low latitudes and slightly elongated in the latitudinal direction. In all panels of Fig. 3 we find concentration of waves in regions corresponding to that of under the Atlantic ($\approx 0°$ E), under the Pacific ($\approx -130°$ E) and under Indonesia ($\approx 120°$ E). These patterns show a westward propagation and are mostly visible in the

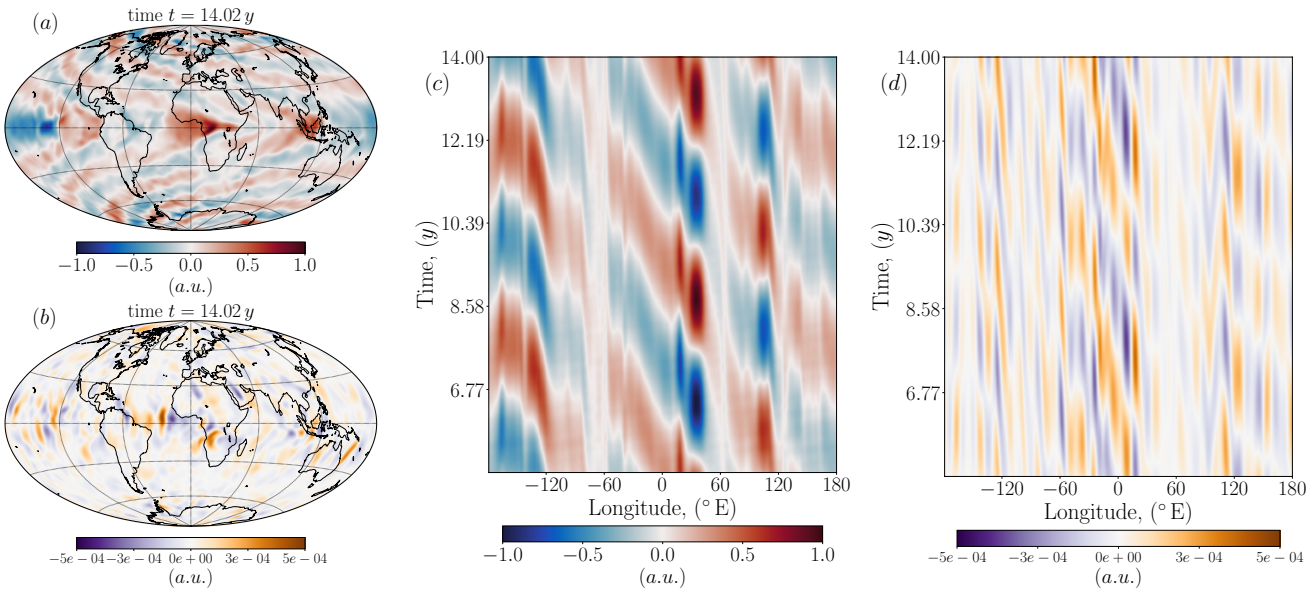

Figure 3: Snapshots of the non-axisymmetric azimuthal perturbation velocity field $u_\phi - \frac{1}{2\pi}\int_0^{2\pi} u_\phi \, \mathrm{d}\phi$ at the outer boundary (a), of the radial perturbation magnetic field b_r at the outer boundary (b), and time-azimuthal plots of the non-axisymmetric azimuthal perturbation velocity field $u_\phi - \frac{1}{2\pi}\int_0^{2\pi} u_\phi \, \mathrm{d}\phi$ at the equator (c), and of the radial perturbation magnetic field b_r at the equator (d), for Case CB-1 using the complex magnetic background field and an input period corresponding to $T_i = 4.4\,\mathrm{y}$. Note that the velocities have been normalised by their respective maximum value and that both the velocity and the magnetic fields have arbitrary units.

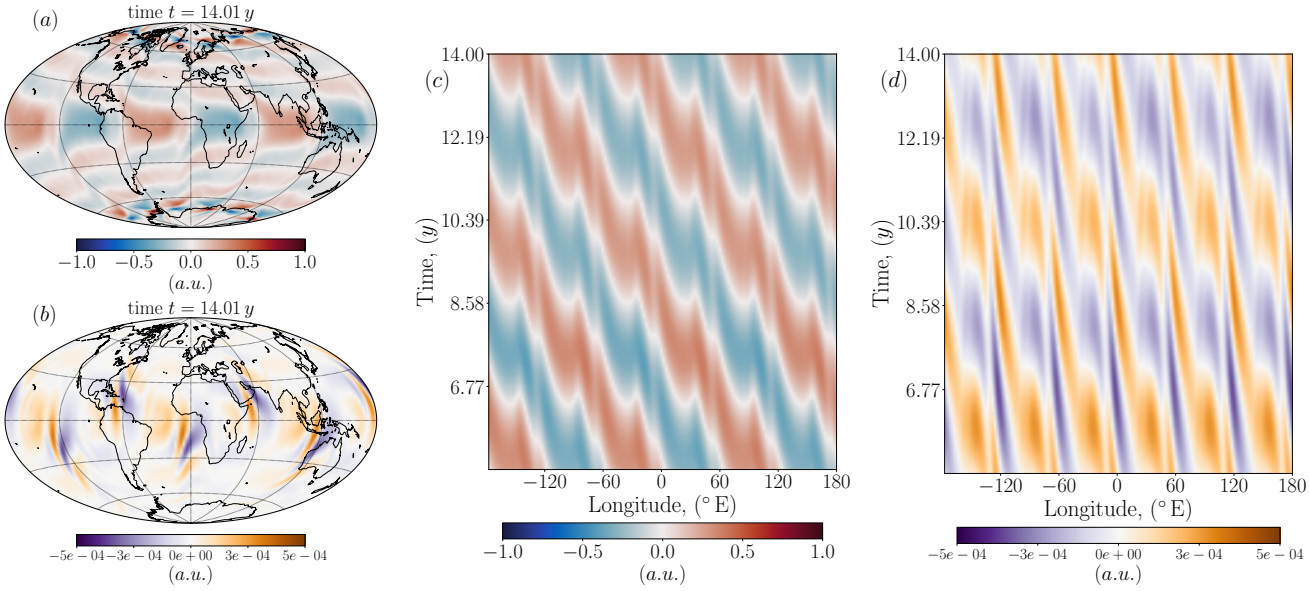

Figure 4: Same as Figure 3 for Case SB-1 using a simple magnetic background field and an input period corresponding to $T_i = 4.4\,\mathrm{y}$.

equatorial regions for both the azimuthal velocity and the radial magnetic fields, an observation that is very clear in the time-azimuth diagrams for both quantities (Fig. 3 c-d). Notice that for this CB-1 case, we have tested a change in the parity and the mode number of the harmonic of the perturbation (using a $\ell = m = 2$ harmonic in Eq. 1) and have recovered the same results (see Fig. 9 in Appendix A.2) which we therefore consider to be generic as long as the perturbation remains sectorial and large scales.

The same observations can be made for Case SB-1, this time using the idealised background state introduced in Barrois and Aubert, 2024 (Fig. 1) and an input period also corresponding to $T_i = 4.4\,\mathrm{y}$. Despite the simplicity of this simpler background state, similar wedged patterns that focus at the equator (Fig. 4 a), the characteristic latitudinal shapes (Fig. 4 b) and the westward propagation (Fig. 4 c-d) can be retrieved again. However, compared to the complex case, the patterns are perfectly regular, do not show regional heterogeneities and the features of the QG-MC waves appear more clearly, especially in the radial magnetic field where the QG-MC waves take the form of latitudinally elongated patches that converge toward the equator (Fig. 4 b).

Conversely, Case CB-2, using the complex magnetic field background and a shorter input period corresponding to $T_i = 0.6\,\mathrm{y}$ (Fig. 5), does not display the same characteristics as the two former cases. The patterns at the CMB are restricted to a thinner equatorial band and are located in a region corresponding to that of under South America ($\approx -90°$ E, Fig. 5 a-

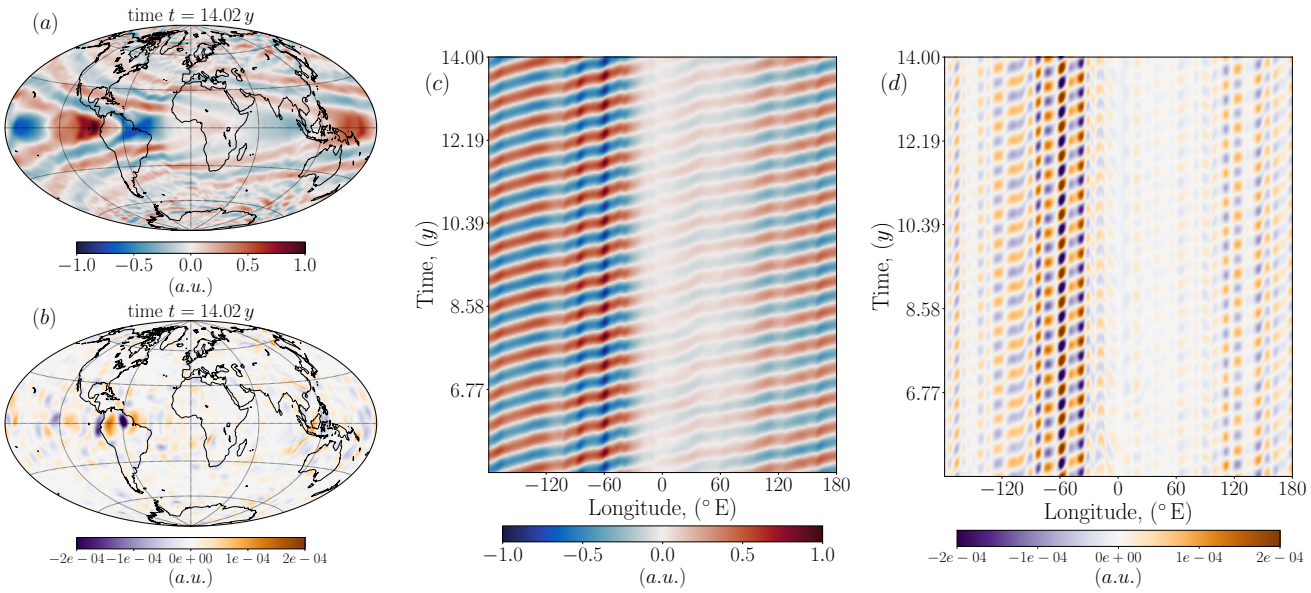

Figure 5: Same as Figure 3 for Case CB-2 using the complex magnetic background field and an input period corresponding to $T_i = 0.6$ y.

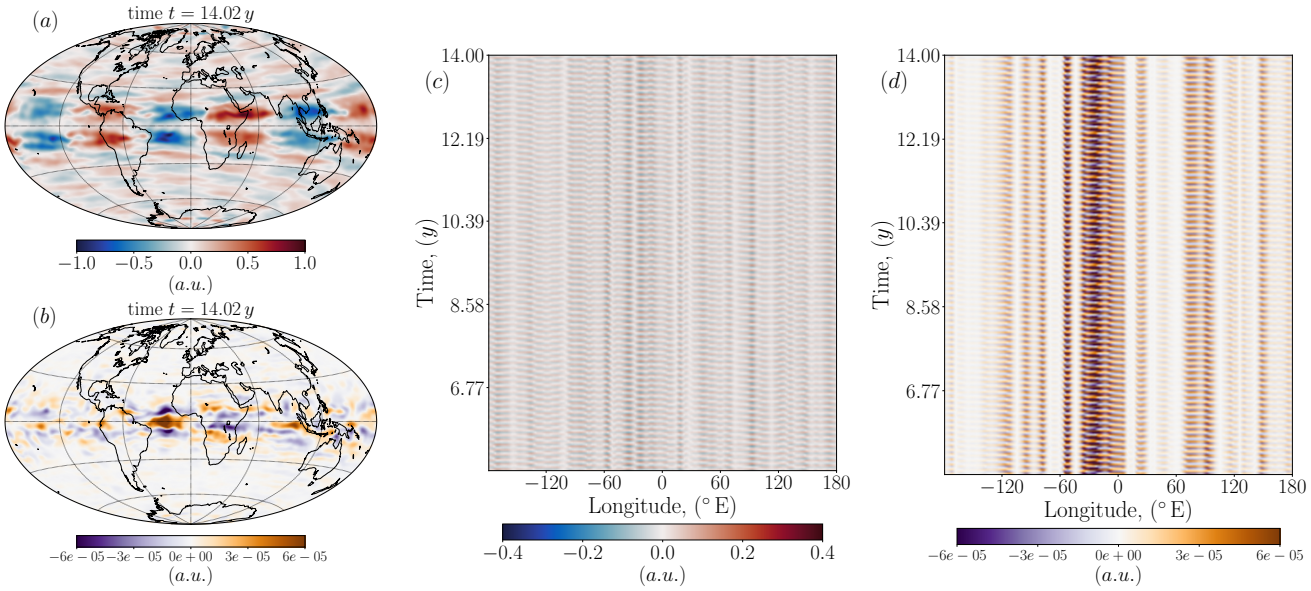

Figure 6: Same as Figure 3 for Case CB-3 using the complex magnetic background field and an input period corresponding to $T_i = 0.06$ y $\approx$ 22 d.

b). Moreover, we observe instead a slow eastward drift in both the velocity and the magnetic fields (Fig. 5 c-d). Therefore, the waves recovered at the CMB using this shorter input period are probably no longer QG-MC waves but likely QG-Alfvén waves mainly because the azimuthal pattern in Fig. 5 (c) appears more simple and regular than the other cases and we expect a transition from QG-MC to QG-Alfvén as the input input period decreases (see Barrois and Aubert, 2024, for details about the waves that can be generated in this reduced setup).

Finally, at the highest explored frequency of Case CB-3, using the complex magnetic field background and an even shorter input period of $T_i = 0.06$ y $\approx$ 22 d (Fig. 6), we find patterns at the CMB that only arise at low latitudes and display a rather perfect azimuthal symmetry of $m = 3$, though this is less clear in the radial magnetic field (Fig. 6 a-b), while we observe a slight westward drift in both the velocity and the magnetic fields, although some eastward drifts can be seen at some longitudes (Fig. 6 c-d). Thus, because of the low amplitude of the radial magnetic field at the CMB (compare the amplitudes of, *e.g.*, Fig. 3 b and Fig. 6 b) and the fact that the waves are confined to a small band at low latitudes – consistent with a propagation of the waves in the ϕ-direction – and, again, because we expect a transition from QG-Alfvén to inertial waves as the input frequency increases (Barrois and Aubert, 2024), we can deduce that the waves observed using this higher input frequency are likely inertial waves.

Comparison of Fig. 3 and 4 indicates that QG-MC waves are weakly sensitive to the details of the background state, and remain clearly observable at the core surface even when using a complex background magnetic field. It appears easier to observe the QG-MC waves in the velocity field, rather than in the magnetic field, in the more complex case, a conclusion already drawn by Gillet, Gerick, Jault, et al., 2022.

In addition, we can see that the QG-MC wave patterns in the radial magnetic field of the complex case (Fig. 3 b-d) have distinct features in the Pacific and the Atlantic hemispheres, especially compared with the patterns of the simple case where the QG-MC waves look similar all over the core surface (Fig. 4). For example, we can observe the concentration of waves below the Atlantic in the magnetic field of the complex case (Fig. 3 b-and-d) similarly to what have been reported for some of the jerks of the satellite observation era, like the 2007 jerk which also focuses at these longitudes (Chulliat et al., 2010; Chulliat et al., 2015; Aubert and Finlay, 2019). These results suggest that the waves carry information about the background magnetic field – at least close to the CMB – and that they might also carry information about the deep state of the magnetic field. From these observations, we can guess that the Pacific region might be more suitable for recovering QG-MC waves in the geomagnetic time series due to the weaker secular variation signal in the Pacific hemisphere, allowing for a clearer separation between the signals from the waves and those from other processes.

3.2 Force balance

In Figure 7, we show nine time-cylindrical radius diagrams of axially-averaged and curled forces that sustain the waves as they travel through the outer core in the three cases: Case CB-1 using the complex background magnetic field and an input period also corresponding to $T_i = 4.4\,\mathrm{y}$ (Fig. 7 a–c), Case SB-1 using the simple background magnetic field and an input period corresponding to $T_i = 4.4\,\mathrm{y}$ (Fig. 7 d–f), and Case CB-2 using the complex background magnetic field and an input period also corresponding to $T_i = 0.6\,\mathrm{y}$ (Fig. 7 g–i).

With a forcing period of $T_i = 4.4\,\mathrm{y}$ and regardless of the background magnetic field, we immediately see that inertia only plays a marginal role in Cases SB-1 and CB-1 and that only the Lorentz and the Coriolis forces are involved in the force balance, unequivocally characterising QG-MC waves (Fig. 7 a–f). This is consistent with what has already been reported in our previous study, using a different initial setup (Barrois and Aubert, 2024), but here the torsional Alfvén waves are absent due to the non-axisymmetric nature of the forcing in this work. It is clear that QG-MC waves arise at the top of the core with a defined temporal and spatial wavelength, even if the propagation of the waves in the bulk is more complex and disturbed when using a realistic background state (Fig. 7 a–c). Note that in all cases, the observed period of the QG-MC waves at the top of the core remains close to that of the input period.

At a faster input period $T_i = 0.6\,\mathrm{y}$ in Case CB-2, we can observe that all three quantities are involved and that a balance between inertia and the Lorentz force – characterising QG-Alfvén waves – dominates the signals (Fig. 7 g–i). QG-MC waves remain present in the simulation – as revealed by the subsisting balance between the Lorentz and Coriolis forces – but they seem to propagate inward similarly to the QG-Alfvén waves and we do not clearly observe outward propagating QG-MC waves. In fact, at this higher frequency, QG-MC waves begin to be superseded by inward QG-Alfvén waves and the latter will be retrieved at the core surface in the components of the fields as it has already been observed in Fig. 5 (a–d).

Note that at the highest input frequency of Case CB-3, we have found that the Coriolis force dominates the balance (not shown) confirming that the waves retrieved in that case are inertial waves.

The results from Fig. 3 and Fig. 7 clearly indicate that the input frequency of the initial perturbation is instrumental in controlling the resulting waves that can be recovered at the core mantle boundary. Therefore, we conclude that there is a constrained range of possible forcing frequencies for the QG-MC waves to be detectable at the core surface. This range varies with the background magnetic field intensity but does not change dramatically with the background state complexity.

3.3 Dispersion relation

Under the plane-wave ansatz and with the following assumptions: (i) the magnetic dissipation is negligible, (ii) the radial wavelength of the perturbation is much shorter than the length-scales over which the medium evolves, (iii) the azimuthal magnetic field is not significantly larger than the radial one, (iv) and the radial length-scales are much shorter than the horizontal length-scales, Gillet, Gerick, Jault, et al., 2022 have proposed a dispersion relation, correlating the pulsation of a wave ω to its cylindrical radial wavenumber k_s, for QG-Alfvén and QG-MC waves which can be written

$$\omega = v_{\mathcal{A}} k_s \left(\left(\frac{k_0}{k_s} \right)^3 \pm \sqrt{1 + \left(\frac{k_0}{k_s} \right)^6} \right), \tag{2}$$

making use of k_0, a radial wavenumber above which only Alfvén waves exist, and below which QG-MC waves can be separated from Rossby waves, reading

$$k_0 = \left(\frac{m\Omega}{v_{\mathcal{A}} h^2} \right)^{1/3}, \tag{3}$$

where m is the azimuthal wavenumber of the excitation source and $h \equiv \sqrt{s_{\mathrm{CMB}}^2 - s^2}$ is the half-height of a cylinder aligned with the rotation axis at a cylindrical radius s. The expression above implies that the transition between the QG-MC and the QG-Alfvén waves is controlled by the base state because this number k_0 depends on the Alfvén velocity $v_{\mathcal{A}}$, which itself depends on the strength of the equatorial background magnetic field $B_{0,s}$, as

$$v_{\mathcal{A}}(s, \phi) \equiv \sqrt{\frac{1}{2h\rho\mu} \int_{-h}^{h} B_{0,s}^2 \, \mathrm{d}z}. \tag{4}$$

In the limit of small wavelengths ($k_s \gg k_0$), we recover the first order of the dispersion relation and the waves frequencies only weakly depart from the Alfvén wave frequency, *i.e.*

$$\omega_{\mathcal{A}} \simeq \pm v_{\mathcal{A}} k_s + \frac{m\Omega}{k_s^2 h^2}, \tag{5}$$

while in the opposite limit ($k_s \ll k_0$), we can separate the inertial Rossby waves,

$$\omega_{\mathrm{R}} = \frac{2m\Omega}{k_s^2 h^2}, \tag{6}$$

and the QG-MC waves, with the latter's frequency being

$$\omega_{\mathrm{MC}} = -\frac{v_{\mathcal{A}}^2 h^2 k_s^4}{2m\Omega}, \tag{7}$$

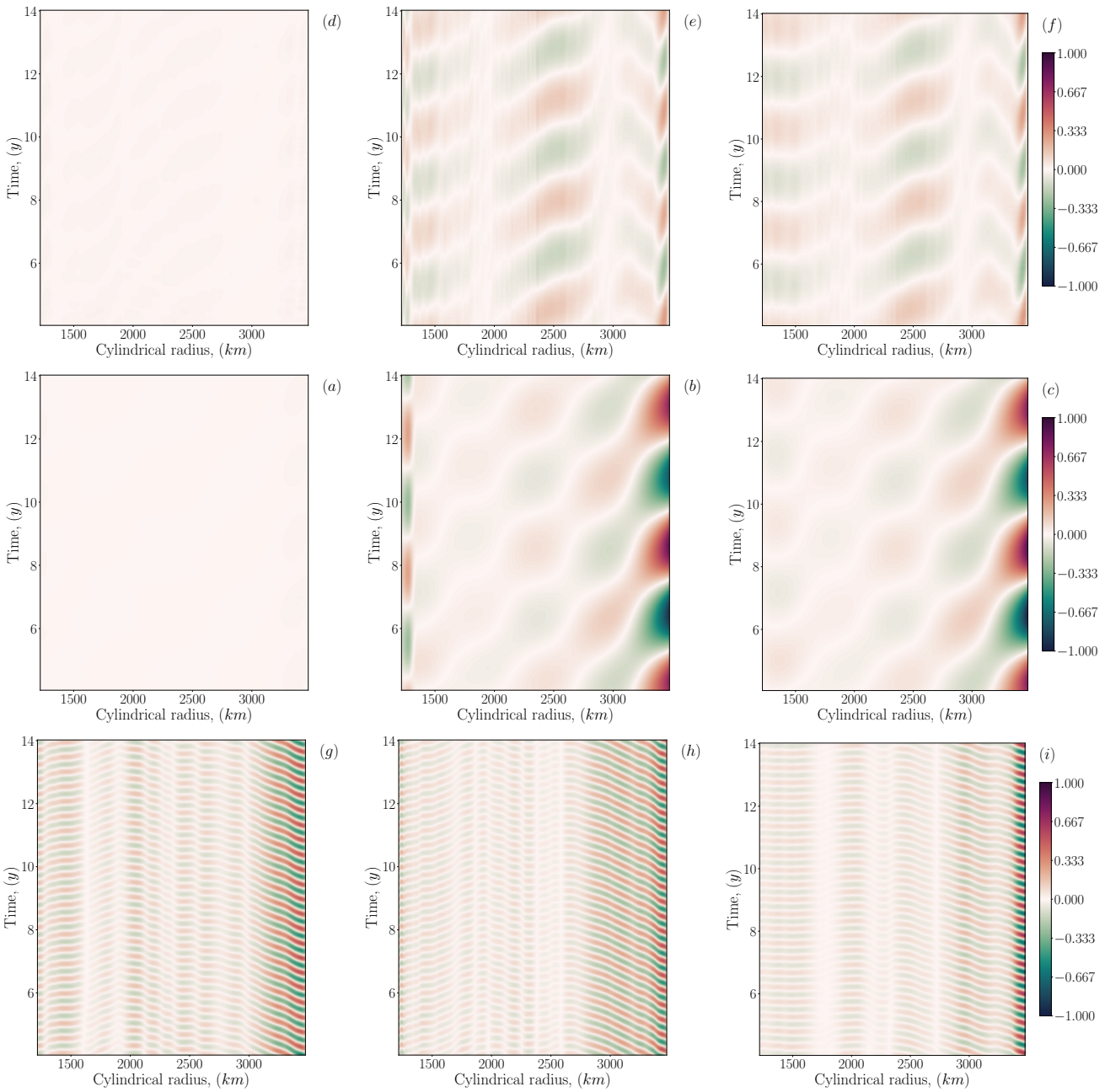

Figure 7: Temporal evolution of the z-averaged and curled inertia (left column), Lorentz force (middle column) and Coriolis force (right column) for Case CB-1 using an input period corresponding to $T_i = 4.4\,\mathrm{y}$ (panels a–c), for Case SB-1 also using an input period corresponding to $T_i = 4.4\,\mathrm{y}$ (panels d–f), and for Case CB-2 using an input period corresponding to $T_i = 0.6\,\mathrm{y}$ (panels g–i). The force balance is taken at a particular 'fast' longitude corresponding to where $B_{0,s}$ is the densest. Note that all forces have been normalised by the maximum value of the Coriolis force for each case.

(Gillet, Gerick, Jault, et al., 2022). Note that Eq. (3) reveals that the increasing azimuthal order m of the excitation source and the increasing strength of the background magnetic field have opposing effects on k_0, because m and $v_{\mathcal{A}}$ are respectively at the numerator and the denominator of this expression, so it is not trivial to anticipate the effect of using a more complex background magnetic field on the transition between the QG-MC and the QG-Alfvén waves from this dispersion relation (as a complex base state allows for coupling between all azimuthal wavenumbers and may yield non-trivial Alfvén speed profiles).

Interestingly in our setup, we actually recover QG-MC waves (see Fig. 3 a-b and Fig. 7 a–c) and inward QG-Alfvén waves (see Fig. 5 a-b and Fig. 7 g–i), while we found slow Rossby waves in our previous study (see, *e.g.*, Fig. 5 of Barrois and Aubert, 2024). However, these slow Rossby waves are transients and therefore not part of the periodic response once the steady state has been reached, though periodic inertial waves are recovered at even higher frequencies (see Fig. 6 a-b). So we partially retrieve the components of the dispersion relation (Eq. 2): *i.e.*, respectively, the ω^- branch corresponding to the slow MC modes (Eq. 7) and the ω^+ or the ω^- branch corresponding to Alfvén modes at higher k_s (Eq. 5). Whilst it is already noteworthy to have qualitatively retrieved and characterised most of the complexity of the system, it is genuinely difficult to produce an accurate full spectral analysis of the cylindrical radial wavenumber k_s over the full range of frequencies $\omega/(2\pi)$ because of

the non-trivial effects of the spherical geometry, of the non-periodicity of the radial axis, and of the smaller and smaller spatial scales involved as the input pulsation is increased.

We thus examine the dispersion relation for QG-MC waves and QG-Alfvén waves only in Figure 8 which displays the evolution of the wave's frequency $|\omega_o|/2\pi$ as a function of its cylindrical radial linear wavenumber $|k_s|/2\pi$ – where the cylindrical radial wavenumbers have been determined from zero-crossings of the z-averaged non-axisymmetric azimuthal velocity component in the s-direction when approaching the core mantle boundary – for several series of cases using both the simple and the complex background magnetic fields. We find that the slow frequencies (bottom left of Fig. 8) are consistent with QG-MC wave properties, *i.e.* the dispersion relation Eq. (7) and Figs. 3, 4, 7 (a–f). At higher frequencies (top right of Fig. 8) both curves flatten which is coherent with the properties of QG-Alfvén waves, *i.e.* Eq. (5) and Figs. 5, 7 (g-i). In addition, we can see that the dispersion relation follows the same evolution in both the S and C cases although the 'inflexion point' of each curve is different due to the variation of k_0 with the intensity of the background magnetic field. We can indeed observe that the transition from a k_s^4 to a k_s^1 slope in Fig. 8 occurs between $k_s/2\pi \approx 3\times10^{-3}$ and $7\times10^{-3}\,\mathrm{km}^{-1}$ which is consistent with $k_0/2\pi$ having a value of $2.91\times10^{-3}\,\mathrm{km}^{-1}$ in the C Cases configuration, and a value of $3.17\times10^{-3}\,\mathrm{km}^{-1}$ in the S Cases configuration. These observations assert that the dispersion relation derived in Gillet, Gerick, Jault, et al., 2022 is a satisfactory approximation. It also confirms that the QG-MC waves that can arise at the top of the core have a restricted frequency range.

Thus, our results imply that there is a frequency window for observing the QG-MC waves at the Earth's core surface. From the complex cases of Fig. 8, we can estimate that signals with a periodicity much shorter than $\simeq 2.8$ y will be QG-Alfvén waves. Note that we were unable to recover the dispersion relation for periodicities longer than $\simeq 57$ y, mainly because the increasing cylindrical radial wavelengths (decreasing wavenumbers) of the QG-MC waves get longer than the size of the modeled shell. In the opposite limit, the determination of radial wavenumbers at high frequency is extremely difficult and our method does not have the required accuracy to track modes with $|k_s|/(2\pi) > 10^{-2}\,\mathrm{km}^{-1}$.

4 Discussion

This study confirms that QG-Alfvén and QG-MC waves can be sustained by a variety of non-axisymmetric background magnetic fields. The non-axisymmetric monochromatic periodic forcing of our model generates QG-MC waves and complex interactions at the core surface produce inward propagating QG-Alfvén waves, as previously observed in a different setup (Barrois and Aubert, 2024). The predominance of one type of wave rather than the other directly depends on the input frequency of the perturbation in the simulations. In the limit of large wavelengths ($k_s \ll k_0$), corresponding to low input frequencies, QG-MC waves are recovered at the CMB, and in the opposite limit of small wavelengths ($k_s \gg k_0$), corresponding to higher input frequencies, QG-Alfvén waves arise at the top of the core and supersede QG-MC waves. From the complex background magnetic field cases, we estimate that QG-MC waves with periods longer than $\gtrsim 2.8$ y can in principle be observable at the top of the Earth's core, while waves at the CMB with periods much shorter than $\ll 2.8$ y are likely QG-Alfvén waves. Note that in our configuration, waves with periods much longer than $\simeq 57$ y become hard to recover (which exceed in any case the high resolution geomagnetic temporal series we currently have access to).

The wavenumber k_0 is thus a crucial parameter as it affects the possibility of detecting the QG-MC or the QG-Alfvén waves. In particular, k_0 could be large enough so that the potential QG-Alfvén waves arising at the Earth's core surface would have too small spatial length-scales and/or too high frequencies to be detectable in the geomagnetic signal. Also, we retrieve inward propagating Alfvén waves in our configuration which might indicate a jump to the ω^+ branch of the dispersion relation (Eq. 2) rather than a mere transition from QG-MC to QG-Alfvén waves on the same ω^- branch of Eq. (7) and Eq. (5) – albeit we fell short of acquiring data for accurately tracking the different branches –, and though we can guess that the non-trivial effects of the spherical geometry could induce a complex transition from the ω^- to the ω^+ branch (similarly to the symmetry breaking observed for torsional waves, as in Cox et al., 2014; Lalloz et al., 2025), an other study focusing on the interactions and reflections of the retrieved QG-MC and QG-Alfvén waves is required to provide a more detailed physical explanation of this transition. Future studies that would test different harmonics at smaller length-scales for the initial perturbation or that would extract a base of QG-MC modes could also be interesting.

The extent of the frequency range where QG-MC waves can arise at the core surface mainly depends on the strength of the background magnetic field, and our consideration of both simple and complex background magnetic fields shows that their geometry do not dramatically change our conclusions, as long as they remain non-axisymmetric (Gerick and Livermore, 2024). This is encouraging for geomagnetic data assimilation (*e.g.*, Lesur et al., 2022; Istas et al., 2023) and for predicting the magnetic field evolution such as with the International Geomagnetic Reference Field (IGRF, Alken et al., 2021) because the robustness of our results against changes in the background state holds the promise of increasing the predictive power of models based on QG-MC wave patterns analysis. However, because the CMB signature of QG-MC waves is only marginally affected by the base state, concerns can be raised for capturing insights on the deep structures of the magnetic field in the outer core as hoped by *e.g.*, Gillet, Gerick, Jault, et al., 2022. Although, the QG-MC waves probably retain probing capabilities as they are channeled by the dense regions of $B_{0,s}$ and we have seen in the geophysical complex magnetic background cases that regional heterogeneities reminiscent of recently observed geomagnetic jerks are retrieved at the core surface. These results suggest that the QG-MC waves at least provide insights on the magnetic field near the core surface and that the information they might carry on the deep state of the magnetic field remains to be refined.

As a final note, the study of waves to probe the Earth's deep layers (see *e.g.*, Gillet, Gerick, Angappan, et al., 2022; Triana et al., 2022; Schwaiger et al., 2024), and the use of reduced models are applicable to a variety of systems and could also bring knowledge to other celestial bodies from

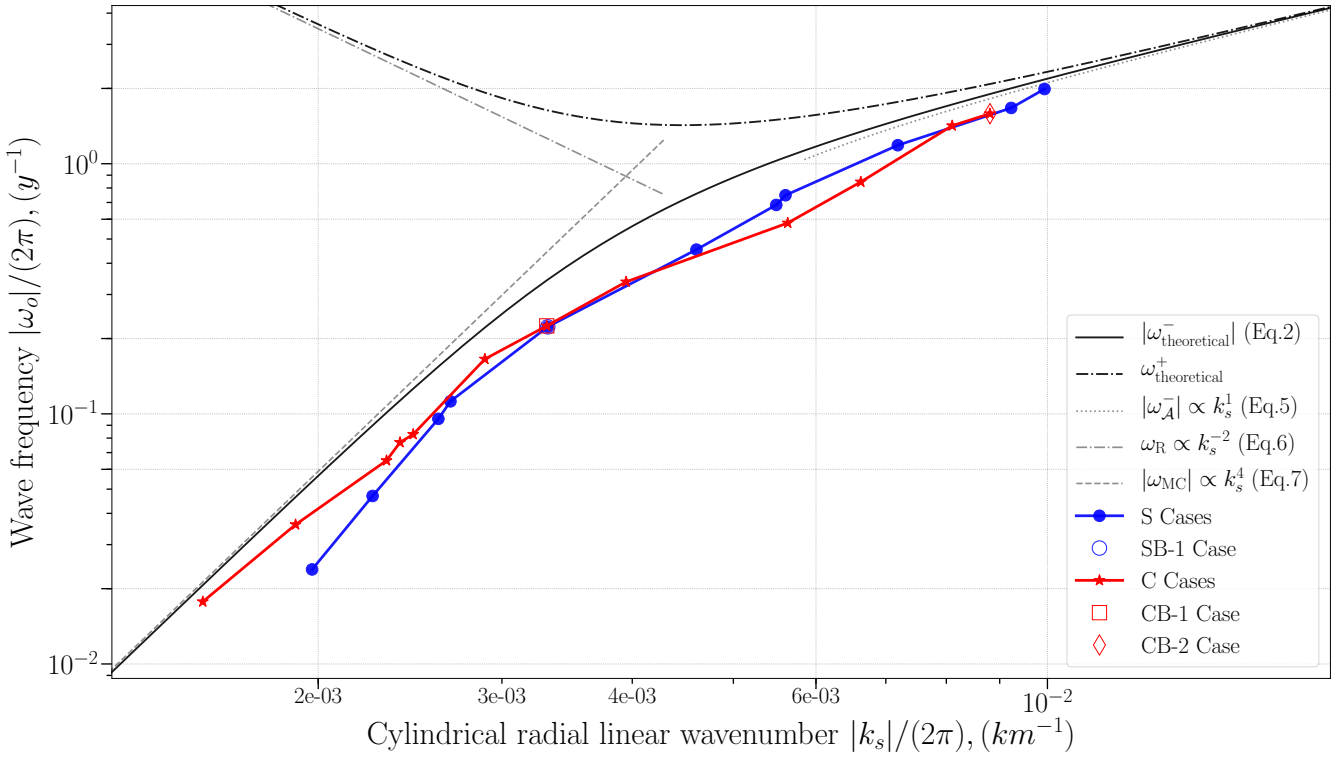

Figure 8: Evolution of the cylindrical radial linear wavenumber $|k_s|/(2\pi)$ as a function of the frequency $|\omega_o|/(2\pi)$, *i.e.* observed dispersion relation of the QG-MC – QG-Alfvén waves in our system for several cases computed at high rotation rate and low attenuation using a simple background magnetic field (blue dots), and the complex background magnetic field (red stars) – note that the symbols for the SB-1 and CB-1 cases are superimposed. Theoretical slopes derived from the dispersion relation and corresponding to Eqs. (2-5-6-7) are also displayed on this figure (various black curves).

which geophysical signals are currently recorded by satellites in the framework of spacecraft missions such as, for example, the JUNO mission (Bolton et al., 2010) with perspectives for finding torsional Alfvén waves or to probe the deep layers of Jupiter (see *e.g.*, Hori et al., 2023) which have been fulfilled with the recent discovery of a periodic oscillation interpreted as a possible torsional wave or localized Alfvén wave in Jupiter's metallic interior (Bloxham et al., 2024).

Acknowledgements

We thank two anonymous reviewers and the editor, Pr. Mathieu Dumberry, for their constructive comments that helped us to improve this manuscript. O. Barrois has received funding from the European Research Council (ERC) **GRACEFUL** Synergy Grant No. 855677. We are grateful to Mioara Mandea for fruitful discussions within the course of this project. Numerical computations were performed on the S-CAPAD platform, IPGP, France.

Data availability

The python package `parobpy` and the scripts used to produce the results shown in this manuscript are available at https://github.com/OBarrois/parobpy.

Competing interests

The authors have no competing interests.

References

Alken, P., E. Thébault, C. D. Beggan, H. Amit, J. Aubert, J. Baerenzung, T. Bondar, W. Brown, S. Califf, A. Chambodut, et al. (2021). International geomagnetic reference field: The thirteenth generation. *Earth Planets Space* 73, 1–25. DOI: 10.1186/s40623-020-01288-x.

Aubert, J. (2019). Approaching Earth's core conditions in high-resolution geodynamo simulations. *Geophys. J. Int.* 219, S137–S151. DOI: 10.1093/gji/ggz232.

Aubert, J. (2020). Recent geomagnetic variations and the force balance in Earth's core. *Geophys. J. Int.* 221, 378–393. DOI: 10.1093/gji/ggaa007.

Aubert, J. (2023). State and evolution of the geodynamo from numerical models reaching the physical conditions of Earth's core. *Geophys. J. Int.* 235, 468–487. DOI: 10.1093/gji/ggad229.

Aubert, J. and C. C. Finlay (2019). Geomagnetic jerks and rapid hydromagnetic waves focusing at Earth's core surface. *Nat. Geosci.* 12, 393–398. DOI: 10.1038/s41561-019-0355-1.

Aubert, J., T. Gastine, and A. Fournier (2017). Spherical convective dynamos in the rapidly rotating asymptotic regime. *J. Fluid Mech.* 813, 558–593. DOI: 10.1017/jfm.2016.789.

Aubert, J. and N. Gillet (2021). The interplay of fast waves and slow convection in geodynamo simulations nearing Earth's core conditions. *Geophys. J. Int.* 225, 1854–1873. DOI: 10.1093/gji/ggab054.

Bärenzung, J., M. Holschneider, J. Wicht, S. Sanchez, and V. Lesur (2018). Modeling and Predicting the Short-Term

Evolution of the Geomagnetic Field. *J. Geophys. Res. Solid Earth* 123, 4539–4560. DOI: 10.1029/2017JB015115.

Barrois, O., M. Hammer, C. Finlay, Y. Martin, and N. Gillet (2018). Assimilation of ground and satellite magnetic measurements: inference of core surface magnetic and velocity field changes. *Geophys. J. Int.* 215, 695–712. DOI: 10.1093/gji/ggy297.

Barrois, O. and J. Aubert (2024). Characterization of hydromagnetic waves propagating over a steady, non-axisymmetric background magnetic field. *Proc. R. Soc. Lond. A*. Vol. 480. The Royal Society, p. 20240067. DOI: 10.1098/rspa.2024.0067.

Bloxham, J., H. Cao, D. J. Stevenson, J. E. Connerney, and S. J. Bolton (2024). A rapidly time-varying equatorial jet in Jupiter's deep interior. *Nature* 627, 64–66. DOI: 10.1038/s41586-024-07046-3.

Bolton et al., S. J. (2010). The juno mission. *Proc. Int. Astro. Union* 6, 92–100. DOI: 10.1007/s11214-017-0429-6.

Buffett, B. and H. Matsui (2019). Equatorially trapped waves in Earth's core. *Geophys. J. Int.* 218, 1210–1225. DOI: 10.1093/gji/ggz233.

Cazenave, A., J. Pfeffer, M. Mandea, V. Dehant, and N. Gillet (2025). Why is the Earth System Oscillating at a 6-Year Period? *Surv. Geophys.*, 1–26. DOI: 10.1007/s10712-024-09874-4.

Chulliat, A. and S. Maus (2014). Geomagnetic secular acceleration, jerks, and a localized standing wave at the core surface from 2000 to 2010. *J. Geophys. Res. Solid Earth* 119, 1531–1543. DOI: 10.1002/2013JB010604.

Chulliat, A., P. Alken, and S. Maus (2015). Fast equatorial waves propagating at the top of the Earth's core. *Geophys. Res. Lett.* 42, 3321–3329. DOI: 10.1002/2015GL064067.

Chulliat, A., E. Thébault, and G. Hulot (2010). Core field acceleration pulse as a common cause of the 2003 and 2007 geomagnetic jerks. *Geophys. Res. Lett.* 37. DOI: 10.1029/2009GL042019.

Cox, G., P. Livermore, and J. Mound (2014). Forward models of torsional waves: dispersion and geometric effects. *Geophys. J. Int.* 196, 1311–1329. DOI: 10.1093/gji/ggt414.

De Wijs, G. A., G. Kresse, L. Vočadlo, D. Dobson, D. Alfe, M. J. Gillan, and G. D. Price (1998). The viscosity of liquid iron at the physical conditions of the Earth's core. *Nature* 392, 805–807. DOI: 10.1038/33905.

Finlay, C. C., C. Kloss, N. Olsen, M. D. Hammer, L. Tøffner-Clausen, A. Grayver, and A. Kuvshinov (2020). The CHAOS-7 geomagnetic field model and observed changes in the South Atlantic Anomaly. *Earth Planets Space* 72, 1–31. DOI: 10.1186/s40623-020-01252-9.

Gerick, F., D. Jault, and J. Noir (2021). Fast quasi-geostrophic Magneto-Coriolis modes in the Earth's core. *Geophys. Res. Lett.* 48, e2020GL090803. DOI: 10.1029/2020GL090803.

Gerick, F. and P. Livermore (2024). Interannual Magneto–Coriolis modes and their sensitivity on the magnetic field within the Earth's core. *Proc. R. Soc. Lond. A*. Vol. 480. The Royal Society, p. 20240184. DOI: 10.1098/rspa.2024.0184.

Gillet, N., F. Gerick, R. Angappan, and D. Jault (2022). A dynamical prospective on interannual geomagnetic field changes. *Surv. Geophys.* 43, 71–105. DOI: 10.1007/s10712-021-09664-2.

Gillet, N., D. Jault, and C. Finlay (2015). Planetary gyre, time-dependent eddies, torsional waves, and equatorial jets at the Earth's core surface. *J. Geophys. Res. Solid Earth* 120, 3991–4013. DOI: 10.1002/2014JB011786.

Gillet, N., F. Gerick, D. Jault, T. Schwaiger, J. Aubert, and M. Istas (2022). Satellite magnetic data reveal interannual waves in Earth's core. *Proc. Nat. Acad. Sci. USA* 119, e2115258119. DOI: 10.1073/pnas.2115258119.

Gillet, N., D. Jault, E. Canet, and A. Fournier (2010). Fast torsional waves and strong magnetic field within the Earth's core. *Nature* 465, 74–77. DOI: 10.1038/NATURE09010.

Gillet, N., N. Schaeffer, and D. Jault (2011). Rationale and geophysical evidence for quasi-geostrophic rapid dynamics within the Earth's outer core. *Phys. Earth Planet. Inter.* 187, 380–390. DOI: 10.1016/j.pepi.2012.03.006.

Hori, K., C. A. Jones, A. Antunano, L. N. Fletcher, and S. M. Tobias (2023). Jupiter's cloud-level variability triggered by torsional oscillations in the interior. *Nat. Astr.* 7, 825–835. DOI: 10.1038/s41550-023-01967-1.

Istas, M., N. Gillet, C. Finlay, M. Hammer, and L. Huder (2023). Transient core surface dynamics from ground and satellite geomagnetic data. *Geophys. J. Int.* 233, 1890–1915. DOI: 10.1093/gji/ggad039.

Jault, D. (2008). Axial invariance of rapidly varying diffusionless motions in the Earth's core interior. *Phys. Earth Planet. Inter.* 166, 67–76. DOI: 10.1016/j.pepi.2007.11.001.

Lalloz, S., L. Davoust, F. Debray, and A. Pothérat (2025). Alfvén waves at low magnetic Reynolds number: transitions between diffusion, dispersive Alfvén waves and nonlinear propagation. *J. Fluid Mech.* 1003, A19. DOI: 10.1017/jfm.2024.1165.

Lesur, V., N. Gillet, M. Hammer, and M. Mandea (2022). Rapid variations of Earth's core magnetic field. *Surv. Geophys.* 43, 41–69. DOI: 10.1007/s10712-021-09662-4.

Nataf, H.-C. and N. Schaeffer (2015). Turbulence in the core. Treatise on geophysics. Vol. 8. Elsevier, pp. 161–181.

Pozzo, M. and D. Alfè (2016). Saturation of electrical resistivity of solid iron at Earth's core conditions. *SpringerPlus* 5, 256. DOI: 10.1186/s40064-016-1829-x.

Pozzo, M., C. Davies, D. Gubbins, and D. Alfè (2014). Thermal and electrical conductivity of solid iron and iron–silicon mixtures at Earth's core conditions. *Earth Planet. Sci. Lett.* 393, 159–164. DOI: 10.1016/j.epsl.2014.02.047.

Rekier, J., B. F. Chao, J. Chen, V. Dehant, S. Rosat, and P. Zhu (2022). Earth's rotation: observations and relation to deep interior. *Surv. Geophys.* 43, 149–175. DOI: 10.1007/s10712-021-09669-x.

Rosat, S. and N. Gillet (2023). Intradecadal variations in length of day: Coherence with models of the Earth's core dynamics. *Phys. Earth Planet. Inter.* 341, 107053. DOI: 10.1016/j.pepi.2023.107053.

Schaeffer, N. (2013). Efficient spherical harmonic transforms aimed at pseudospectral numerical simulations. *Geochem. Geophys. Geosyst.* 14, 751–758. DOI: 10.1002/ggge.20071.

Schwaiger, T., N. Gillet, D. Jault, M. Istas, and M. Mandea (2024). Wave-like motions and torques in Earth's core as inferred from geomagnetic data: A synthetic study. *Phys. Earth Planet. Inter.* 346, 107104. DOI: 10.1016/j.pepi.2023.107104.

Triana, S. A., M. Dumberry, D. Cébron, J. Vidal, A. Trinh, F. Gerick, and J. Rekier (2022). Core Eigenmodes and their Impact on the Earth's Rotation. *Surv. Geophys.*, 1–42. DOI: 10.1007/s10712-021-09668-y.

A Methods details

A.1 Linearised Magneto-hydrodynamic equations

Our reduced system of linearised equations solves for the velocity perturbation $\boldsymbol{u}$ and magnetic perturbation $\mathbf{b}$ fields, with $\mathbf{U} = \mathbf{U}_0 + \boldsymbol{u}$ and $\mathbf{B} = \mathbf{B}_0 + \mathbf{b}$. Note that we actually neglect the background flow $\mathbf{U}_0$ in our model because the background velocity field is believed to be unimportant at the Alfvén timescales for the Earth's core (Gillet et al., 2015; Bärenzung et al., 2018) and the 1st order dynamics is our primary focus. For the same reasons, the 0th order Lorentz force $(\nabla\times\mathbf{B}_0)\times\mathbf{B}_0$ which could drive a background flow is also neglected in our reduced model (which is a classical assumption in such studies, *e.g.*, Gillet et al., 2011; Gerick et al., 2021). It follows that the temporal evolution of the perturbation fields in our models reads

$$\frac{\partial \boldsymbol{u}}{\partial t} + \frac{2}{\lambda}\boldsymbol{e}_z\times\boldsymbol{u} = -\nabla p + \frac{1}{Pm\,\lambda}\left[(\nabla\times\mathbf{b})\times\mathbf{B}_0 + (\nabla\times\mathbf{B}_0)\times\mathbf{b}\right] + \frac{Pm}{S}\nabla^2\boldsymbol{u}, \tag{8}$$

$$\frac{\partial \mathbf{b}}{\partial t} = \nabla\times(\boldsymbol{u}\times\mathbf{B}_0) + \frac{1}{S}\nabla^2\mathbf{b}. \tag{9}$$

Where the perturbations $\boldsymbol{u}$ and $\mathbf{b}$ are triggered by an initial perturbation in the force balance (see section 2.3 and Eq. 1).

Using the Alfvén timescale $\tau_{\mathcal{A}} = d\sqrt{\rho\mu}/B_0$ as the reference for time, where B_0 is the rms value of the background magnetic field, the shell thickness d as the reference for length, and the Elsasser unit $\sqrt{\Omega\eta\rho\mu}$ as the reference for magnetic field strength, where η is the magnetic diffusivity of the fluid, our system is controlled by the dimensionless Lehnert λ, Lundquist S, and magnetic Prandtl Pm numbers, whereas the Ekman number Ek is included as a reference, respectively defined as

$$\lambda = \frac{B_0}{\Omega d\sqrt{\rho\mu}},\ S = \frac{dB_0}{\eta\sqrt{\rho\mu}},\ Pm = \frac{\nu}{\eta},\ Ek = \frac{\nu}{\Omega d^2}, \tag{10}$$

for which their Earth's core estimates are approximately $\lambda \sim O(10^{-4})$, $S \sim O(10^5)$, $Pm \sim O(10^{-6})$ and $Ek \sim O(10^{-15})$ (De Wijs et al., 1998; Gillet et al., 2010; Pozzo et al., 2014), and which can also be expressed as timescales, such that

$$\lambda = \frac{\tau_\Omega}{\tau_{\mathcal{A}}},\ S = \frac{\tau_\eta}{\tau_{\mathcal{A}}},\ Pm = \frac{\tau_\eta}{\tau_\nu},\ Ek = \frac{\tau_\Omega}{\tau_\nu}, \tag{11}$$

where ν is the kinematic viscosity of the fluid, $\tau_\eta = d^2/\eta$ is the magnetic diffusive timescale, $\tau_\nu = d^2/\nu$ is the viscous diffusive timescale, and $\tau_\Omega = 1/\Omega$ is the rotation timescale.

Introducing the Elsasser number Λ, a dimensionless measure of the background magnetic field strength, that is

$$\Lambda = \frac{B_0^2}{\Omega\eta\rho\mu} = \frac{S^2\,Ek}{Pm} = \frac{Ek}{\lambda^2\,Pm}, \tag{12}$$

the simple background field has a dimensionless strength of $\Lambda = 1.77$ and the complex background field has a dimensionless strength of $\Lambda = 3.13$. In both series, we vary the input pulsation of the perturbation from $\tilde{\omega}_i = 0.2$ up to $\tilde{\omega}_i = 25$, with one case using an input pulsation of $\tilde{\omega}_i = 212.3$ (where times are expressed in terms of the dimensionless Alfvén timescale $\tau_{\mathcal{A}}$) while all runs have been computed using $Ek = 1\times10^{-7}$ and $Pm = 0.144$.

A.2 Sensitivity to initial conditions

For a case similar to Case CB-1, using the complex magnetic background field, an input period corresponding to $T_i = 4.4$ y but instead using a spherical harmonic Y_2^2 for the perturbation in Eq. (1), Fig. 9 illustrates that our results are generic as long as the perturbation remains sectorial. We can indeed make the same observations that have been made for Case CB-1 (see Fig. 3 in Section 3.1), with the presence of the characteristic QG-MC patterns focusing at the equator (Fig. 9 a-b), or the clear westward propagation of the waves (Fig. 9 c-d).

A.3 Numerical implementation

The numerical implementation of our model is based on a second-order finite-difference scheme up to a maximum of N_r grid points in the radial direction, and on a spherical harmonic decomposition of the velocity field $\mathbf{U}$ and the magnetic $\mathbf{B}$ field up to a maximum degree and order $\ell_{\max} = m_{\max}$ in the horizontal direction. The spherical harmonic transforms are handled using `SHTns`[1] (Schaeffer, 2013). The Message Passing Interface (`MPI`) library is used for the parallelisation of the code. To time-step the equations of our system, a second-order, semi-implicit scheme is used.

The solutions of our problem are approximated making use of the hyperdiffusivity of the small length-scales of the velocity field, following Nataf and Schaeffer, 2015; Aubert et al., 2017; Aubert, 2019, such that

$$\nu_{\text{eff}} = \nu\, q_H^{\ell-\ell_H} \text{ for } \ell \geq \ell_H, \tag{13}$$

where ℓ_H is the cut-off degree above which the hyperdiffusion smoothly increases and affects the small length-scales of the velocity field, whereas the magnetic field is never affected in our model, and q_H is the parameter controlling the increasing level of the hyperdiffusivity. Values for ℓ_H and q_H have been chosen such that the solutions show a satisfying convergence of the kinetic and magnetic energy spectra. To test the convergence of our solutions, the hyperdiffusion parameters have been varied in a series of different cases and we have not observed any major changes in the average properties (see our previous study Barrois and Aubert, 2024, for more details). Note that in this study, we have used a fixed strength $q_H = 1.05$, a fixed cut-off harmonic degree $l_H = 30$ for the hyperdiffusion, and a fixed grid-size of $(N_r, \ell_{\max}) = (450, 133)$.

[1] https://bitbucket.org/nschaeff/shtns

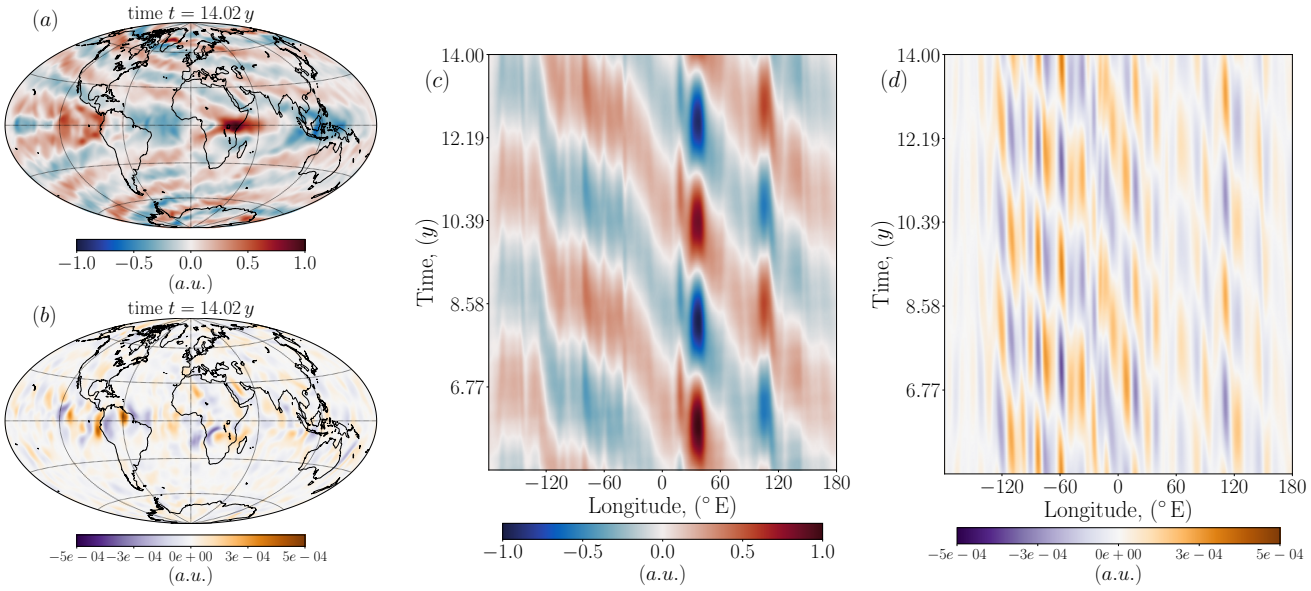

Figure 9: Same as Figure 3 for a case similar to Case CB-1 using the complex magnetic background field and an input period corresponding to $T_i = 4.4\,\mathrm{y}$ but using a spherical harmonic Y_2^2 in space for the periodic perturbation (Eq. 1).

B Results of numerical simulations

Table 1: Summary of the numerical simulations computed in this study using $r_i/r_o = 0.35$ as suited for the Earth's core. In the first column, the letter S denotes the runs using a simple background magnetic field, the letter C denotes the runs using a geophysical complex background magnetic field, while codes such as SB-1 denote specific cases shown in the main text. S is the Lundquist number, λ is the Lehnert number, Λ is the Elsasser number of the background magnetic field, $\tilde{\omega}_i$ is the dimensionless input pulsation of the perturbation, $\tilde{\omega}_o$ is the dimensionless pulsation of the output waves at the core surface (expressed in terms of the Alfvén timescale $\tau_{\mathcal{A}}$), and $\tilde{k}_{s,o}$ is the output dimensionless cylindrical radial wavenumber of the waves at the core surface. The last column reports which type of wave is observed at the core surface. All runs have been computed using an Ekman number $Ek = 1\times10^{-7}$, a magnetic Prandtl number $Pm = 0.144$, a fixed strength $q_H = 1.05$ and a fixed cut-off harmonic degree $l_H = 30$ for the hyperdiffusion, and a grid-size of $(N_r, \ell_{\max}) = (450, 133)$.

Case	S	λ	Λ	$\tilde{\omega}_i$	$\tilde{\omega}_o$	$\tilde{k}_{s,o}$	Waves at CMB
S	1596	1.11×10^{-3}	1.77	0.292	0.3	28	QG-MC
S	1596	1.11×10^{-3}	1.77	0.585	0.59	32	QG-MC
S	1596	1.11×10^{-3}	1.77	1.170	1.2	37	QG-MC
S	1596	1.11×10^{-3}	1.77	1.428	1.41	38	QG-MC
SB-1	1596	1.11×10^{-3}	1.77	2.856	2.8	47	QG-MC
S	1596	1.11×10^{-3}	1.77	5.712	5.7	65	QG-MC
S	1596	1.11×10^{-3}	1.77	9.359	9.4	80	QG-MC
S	1596	1.11×10^{-3}	1.77	14.28	14.9	102	QG-MC–Alfvén
S	1596	1.11×10^{-3}	1.77	19.99	21.0	131	QG-Alfvén
S	1596	1.11×10^{-3}	1.77	24.28	25.0	141	QG-Alfvén
C	2124	1.48×10^{-3}	3.13	0.217	0.22	22	QG-MC
C	2124	1.48×10^{-3}	3.13	0.435	0.45	27	QG-MC
C	2124	1.48×10^{-3}	3.13	0.869	0.82	33	QG-MC
C	2124	1.48×10^{-3}	3.13	1.061	1.04	35	QG-MC
C	2124	1.48×10^{-3}	3.13	1.170	1.00	34	QG-MC
C	2124	1.48×10^{-3}	3.13	2.123	2.08	41	QG-MC
CB-1	2124	1.48×10^{-3}	3.13	2.856	2.85	47	QG-MC
C	2124	1.48×10^{-3}	3.13	4.245	4.24	56	QG-MC
C	2124	1.48×10^{-3}	3.13	7.429	7.28	80	QG-MC
C	2124	1.48×10^{-3}	3.13	10.61	10.6	94	QG-MC
C	2124	1.48×10^{-3}	3.13	18.04	17.8	115	QG-Alfvén
CB-2	2124	1.48×10^{-3}	3.13	19.99	19.9	125	QG-Alfvén
CB-3	2124	1.48×10^{-3}	3.13	212.3	213.0	/	inertial